AIAA JOURNAL
Vol. 41, No. 7, July 2003

# Optimal Transpiration Boundary Control for Aeroacoustics

S. Scott Collis,* Kaveh Ghayour,† and Matthias Heinkenschloss‡
*Rice University, Houston, Texas 77005-1892*

**We consider the optimal boundary control of aeroacoustic noise, governed by the two-dimensional unsteady compressible Euler equations. The control is the time- and space-varying wall normal velocity on a subset of an otherwise solid wall. The objective functional to be minimized is a measure of acoustic amplitude. Optimal transpiration boundary control of aeroacoustic noise introduces challenges beyond those encountered in direct aeroacoustic simulations or in many other optimization problems governed by compressible Euler equations. One nontrivial issue that arises in the optimal control problem is the formulation and implementation of transpiration boundary conditions. Because suction and blowing on the boundary are allowed, portions of the boundary may change from inflow to outflow, or vice versa, and different numbers of boundary conditions must be imposed at inflow vs outflow boundaries. Another important issue is the derivation of adjoint equations, which are required to compute the gradient of the objective function with respect to the control. Among other things, this is influenced by the choice of boundary conditions for the compressible Euler equations. The approaches to meet these challenges are described and results presented for three model problems. These problems are designed to validate the transpiration boundary conditions and their implementation, study the accuracy of gradient computations, and assess the performance of the computed controls.**

## Nomenclature

| | | |
|---|---|---|
| $\boldsymbol{A}_i$ | = | Jacobian of $\boldsymbol{F}^i$ with respect to $\boldsymbol{u}$ |
| $\boldsymbol{B}$ | = | vector of boundary conditions |
| $c$ | = | speed of sound |
| $E$ | = | total energy per unit mass |
| $\boldsymbol{F}^i$ | = | convective flux in $x_i$ direction |
| $\mathcal{G}_{\text{ad}}$ | = | set of admissible controls |
| $g$ | = | transpiration control on $\Gamma_c$ |
| $H$ | = | stagnation enthalpy |
| $h$ | = | enthalpy |
| $J$ | = | objective function |
| $J_{\text{obs}}$ | = | observation term |
| $J_{\text{reg}}$ | = | regularization term |
| $M$ | = | Mach number |
| $\boldsymbol{n}$ | = | unit outward normal |
| $p$ | = | pressure |
| $p_a$ | = | steady mean flow pressure |
| $\boldsymbol{q}$ | = | conserved variables $[\rho, \rho v_1, \rho v_2, \rho E]^T$ |
| $R$ | = | radius of curvature |
| $S$ | = | entropy |
| $\boldsymbol{s}$ | = | unit tangential vector |
| $T$ | = | temperature |
| $(t_0, t_f)$ | = | time period of interest |
| $\boldsymbol{u}$ | = | primitive variables $[\rho, v_1, v_2, T]^T$ |
| $\boldsymbol{u}_0$ | = | initial condition at $t_0$ |
| $\boldsymbol{v}$ | = | velocity vector, $[v_1, v_2]^T$ |
| $\boldsymbol{x}$ | = | position vector, $[x_1, x_2]^T$ |
| $\alpha_i$ | = | positive weighting parameters |
| $\Gamma$ | = | boundary of $\Omega$ |
| $\Gamma_c$ | = | subset of $\Gamma$ with control actuation |
| $\gamma$ | = | ratio of specific heats |
| $\delta_{ij}$ | = | Kronecker delta |
| $\boldsymbol{\lambda}$ | = | adjoint variables |
| $\boldsymbol{\lambda}^b$ | = | adjoint variables associated with boundary conditions |
| $\boldsymbol{\lambda}^0$ | = | adjoint variables associated with initial conditions |
| $\boldsymbol{\mu}$ | = | adjoint momentum $[\lambda_2, \lambda_3]^T$ |
| $\rho$ | = | density |
| $\chi_{\Omega_{\text{obs}}}$ | = | indicator function |
| $\boldsymbol{\Psi}$ | = | adjoint characteristic variables |
| $\Omega$ | = | spatial domain |
| $\Omega_{\text{obs}}$ | = | observation region |
| $\omega$ | = | vorticity |

Presented as Paper 2002-2757 at the AIAA 3rd Theoretical Fluid Mechanics Meeting, St Louis, MO, 24 June 2002; received 8 July 2002; revision received 28 January 2003; accepted for publication 19 February 2003. 

*Assistant Professor, Department of Mechanical Engineering and Materials Science; collis@rice.edu. Member AIAA.

†Postdoctoral Associate, Department of Computational and Applied Mathematics and Department of Mechanical Engineering and Materials Science; kghayour@caam.rice.edu.

‡Associate Professor, Department of Computational and Applied Mathematics; heinken@rice.edu.

## Introduction

THE goals of this paper are the description of issues arising in the computation of optimal transpiration boundary controls for the minimization of aeroacoustic noise, the introduction of our approaches to deal with these issues, and the presentation of numerical results that support the effectiveness of our approach.

The control objective for aeroacoustic applications usually targets acoustic waves that are typically several orders of magnitude smaller than flow quantities associated with the energetically dominant dynamics. Like the direct simulation of aeroacoustic phenomena, optimal control of aeroacoustics requires proper resolution of small-amplitude acoustic fluctuations. However, optimal control imposes additional demands. First, optimal control of aeroacoustic noise requires that dynamic control actuations are properly translated into small-amplitude acoustic fluctuations. This can add significant challenges to the simulation. Second, to apply gradient based optimization algorithms for the computation of an optimal control, one needs to compute sensitivity information. In our case, where controls are temporally and spatially distributed, this is accomplished with the adjoint equation approach. The implementation of the adjoint equation needs to relate undesired small-amplitude acoustic fluctuations accurately to modifications of the control that can reduce them.

Acoustic waves are nondissipative and nondispersive; their resolution requires high-order accurate numerical schemes with minimal dissipation and dispersion error. In our state computations, spatial derivative operators are discretized with sixth-order central finite differences, and a fourth-order accurate explicit Runge–Kutta scheme is used to advance the solution in time. We use sponge regions near the far-field boundaries to allow acoustic waves and spurious numerical waves to leave the domain without significant

reflections. A nonstandard and nontrivial task that arises in our optimal control problem is the formulation and implementation of transpiration boundary conditions. Because we allow suction and blowing on the boundary, portions of the boundary are allowed to change dynamically from inflow to outflow, or vice versa. Different numbers of boundary conditions have to be imposed depending on whether a boundary portion is an inflow or an outflow boundary. Specifically, for subsonic suction only one physical boundary condition is required, whereas three physical boundary conditions are needed for subsonic blowing. Our choice of boundary conditions, as well as their implementation in the context of our high-order finite difference based code, is discussed hereafter. Our implementation of the boundary conditions borrows heavily from Sesterhenn.[1]

Because the number of control variables in our problem is large, we apply a gradient-based algorithm for the computation of an optimal control. The gradient of the objective function with respect to the control is computed by the adjoint equation approach. The general framework underlying our approach in this paper is the same as that used in previous work,[2,3] and it is similar to many adjoint equation-based optimization procedures used for optimization of unsteady problems. It carefully addresses some subtle but important issues that are sometimes overlooked in other works. In previous work[2] on the optimal boundary control of unsteady, two-dimensional viscous compressible flows, the discretize-then-optimize approach for gradient computation was used. In this approach, the state equation and objective function are first discretized, and the adjoint calculus is applied to the discrete problem, possibly aided by automatic differentiation. Although this method generates exact gradient information for the discretized problem, it does so without providing direct physical and mathematical insight into the adjoint partial differential equations (PDEs), especially their boundary conditions, associated with the continuous problem. The latter are important to assess the well-posed nature of the optimal control problem and the quality of the computed discretized control as an approximation to the true optimal control. Accurate state discretizations are not sufficient to ensure an accurate discretization of the optimal control problem. For the latter, it is also necessary to resolve the adjoint PDEs adequately. Gradient computations using the optimize-then-discretize approach, in which one first determines the adjoint PDEs and their boundary conditions, and then discretizes these, in combination with the aforementioned discretize-then-optimize approach, can provide some insight into the issues of well-posed nature and approximation quality. We present comparisons of gradient information computed using our optimize-then-discretize approach with finite difference gradient information, which corresponds to the discretize-then-optimize approach.

To test our approach, three optimal control problems are solved and discussed in this paper. The first test problem shows that the computed optimal controls can produce well-resolved planar acoustic waves of very small amplitude to minimize the observed sound amplitudes by means of wave cancellation. In the second test problem, the optimal control targets the no-penetration solid wall boundary condition, which amplifies the noise amplitude by reflecting the incident waves back into the observation region. The computed optimal control lets the incident acoustic waves pass through the wall, mimicking a nonreflecting boundary condition. The third and last test problem compares the nonreflecting behavior of the optimal transpiration control against two widely used nonreflecting far-field boundary conditions. The success of this approach has enabled us to investigate the feasibility of optimal transpiration control for reducing the impulsive noise associated with the blade vortex interaction phenomenon in Ref. 4.

## Problem Formulation

### State Equations

The vector $\boldsymbol{u} = (\rho, v_1, v_2, T)^T$ denotes the primitive variables, and $\boldsymbol{q}(\boldsymbol{u}) = (\rho, \rho v_1, \rho v_2, \rho E)^T$ denotes the conserved variables. Here $\rho$, $v_i$, and $T$ are the density, the velocity component in the $x_i$ direction, and the temperature, respectively. The pressure $p$ and total energy per unit mass $E$ are given by

$$p = \rho T/\gamma M^2, \qquad E = [T/\gamma(\gamma-1)M^2] + \tfrac{1}{2}\boldsymbol{v}^T\boldsymbol{v} \tag{1}$$

where $M$ is the reference Mach number. The convective flux in the $x_i$ direction is

$$\boldsymbol{F}^i(\boldsymbol{u}) = \begin{bmatrix} \rho v_i \\ p\delta_{i1} + \rho v_1 v_i \\ p\delta_{i2} + \rho v_2 v_i \\ (p + \rho E) v_i \end{bmatrix} \tag{2}$$

where $\delta_{ij}$ is the Kronecker symbol.

The spatial domain occupied by the fluid is $\Omega \subset \mathbb{R}^2$, the portion of the solid boundary on which control is exercised is $\Gamma_c$, and $(t_0, t_f)$ is the time period of interest. By $\boldsymbol{n} = (n_1, n_2)^T$, we denote the unit outward normal to the boundary $\Gamma$ of $\Omega$. In our model problems, $\Omega = \{\boldsymbol{x} \in \mathbb{R}^2 : x_2 > 0\}$, $\Gamma_c = \{\boldsymbol{x} \in \mathbb{R}^2 : x_2 = 0,\ a \le x_1 \le b\}$, and $\boldsymbol{n} = (0, -1)^T$. The Euler equations can be written in conservative form as

$$\boldsymbol{q}(\boldsymbol{u})_t + \sum_{i=1}^{2} \boldsymbol{F}^i(\boldsymbol{u})_{x_i} = \boldsymbol{0}, \qquad \text{in} \qquad (t_0, t_f) \times \Omega \tag{3a}$$

with boundary conditions

$$\boldsymbol{B}(\boldsymbol{u}, \nabla\boldsymbol{u}, g) = \boldsymbol{0}, \qquad \text{on} \qquad (t_0, t_f) \times \Gamma \tag{3b}$$

and initial conditions

$$\boldsymbol{u}(t_0, \boldsymbol{x}) = \boldsymbol{u}_0(\boldsymbol{x}), \qquad \text{in} \qquad \Omega \tag{3c}$$

The function $g$ in the boundary conditions (3b) is the transpiration boundary control $g = \boldsymbol{v}^T\boldsymbol{n}$, which is to be determined on the controlled boundary $\Gamma_c$. Positive $g$ denotes suction, whereas negative $g$ corresponds to injecting fluid into the domain $\Omega$. The precise form of the boundary conditions (3b) will be specified in the following section.

### Wall Boundary Conditions

Transpiration boundary control $g$ takes place in the near-field region where nonlinearities, unsteadiness, and spatial gradients are often significant. Not surprisingly, implementation of a boundary treatment that can accommodate this control mechanism is not an easy task. Moreover, the hyperbolic nature of the Euler equations (and its discretization) often leads to the propagation of nonphysical error waves associated with inappropriately imposed and/or implemented boundary conditions. This can ultimately contaminate the solution everywhere in the domain. This difficulty is particularly acute for high-order central difference discretizations when mated with explicit time-advancement schemes. The discrete dispersion relation permits highly oscillatory numerical error waves that can propagate faster than the physical waves of the system, often leading to restrictive time-step constraints.

The implementation of slip-wall boundary conditions (zero normal velocity) for aeroacoustic computations has received attention, most notably the ghost cell method of Tam and Dong[5] and Kurbatskii and Tam.[6] However, implementation of transpiration-type boundary conditions for inviscid compressible flows has received relatively less attention. We view the transpiration boundary condition as an inflow/outflow boundary condition, where the number of physical boundary conditions is dictated by the characteristic speeds associated with the unit outward normal $\boldsymbol{n}$. These speeds are $\boldsymbol{v}^T\boldsymbol{n}$ (with a multiplicity corresponding to the space dimension) and $\boldsymbol{v}^T\boldsymbol{n} \pm c$, where $\boldsymbol{v}$ and $c$ are the local velocity and sound speed, respectively. When one of these characteristic speeds is negative, the associated characteristic quantity propagates from outside the boundary toward the interior of the domain, and a physical boundary condition must be imposed. On the other hand, a positive speed indicates flow of information from the inner domain toward the boundary, necessitating the imposition of a numerical boundary condition. Therefore,

one physical and three numerical boundary conditions must be imposed for subsonic suction, and three physical and one numerical boundary conditions are needed for subsonic blowing. Hence, for an impermeable wall or suction, $\boldsymbol{v}^T\boldsymbol{n} \geq 0$, and the physical boundary condition

$$\boldsymbol{v}^T\boldsymbol{n} - g = 0 \tag{4}$$

must be satisfied. However, when fluid is injected into the domain, not only must the wall normal velocity be specified, but, as suggested by the characteristic speeds normal to the boundary, two other flow quantities must be imposed. The appropriate selection of the additional flow quantities that should be constrained can impact both the implementation, as well as the accuracy, of the final method. Based on extensive experimentation, we have selected entropy and vorticity as the additional flow quantities that are specified in our transpiration boundary condition. This was motivated by the well-known fact that entropy and vorticity information propagates along the incoming characteristics, and, as shown hereafter, we were able to implement these boundary conditions within our high-order finite difference discretization in such a way that high accuracy and numerical stability were retained. In summary, for $\boldsymbol{v}^T\boldsymbol{n} < 0$, the boundary conditions

$$\boldsymbol{v}^T\boldsymbol{n} = g, \qquad \ell n\left(T^{1/(\gamma-1)}/\rho\right) = S_0, \qquad \partial_{x_2} v_1 - \partial_{x_1} v_2 = \omega_0 \tag{5}$$

are imposed. In this study, we require the injected fluid to be isentropic and irrotational by setting $\omega_0 = S_0 = 0$. Injection of rotational fluid will be explored in future work.

We may combine Eqs. (4) and (5) into

$$\boldsymbol{B}(\boldsymbol{u}, \nabla\boldsymbol{u}, g) \overset{\text{def}}{=} \begin{Bmatrix} \boldsymbol{v}^T\boldsymbol{n} - g \\ \left[\ell n\left(T^{1/(\gamma-1)}/\rho\right) - S_0\right] \min\{g, 0\}^2 \\ \left(\partial_{x_2} v_1 - \partial_{x_1} v_2 - \omega_0\right) \min\{g, 0\}^2 \end{Bmatrix} = \boldsymbol{0}$$

Although we have used these boundary conditions successfully in several optimal control applications, the mathematically well-posed nature of the compressible Euler equations with these boundary conditions has not been established. Success of these boundary conditions may be dependent on their implementation, which is discussed hereafter.

**Optimal Control Problem**

In this paper, we solve

$$\min_{g \in \mathcal{G}_{\text{ad}}} J(g) \tag{6}$$

where the objective function is defined as

$$J(g) = J_{\text{obs}}(g) + J_{\text{reg}}(g) \tag{7a}$$

$$J_{\text{obs}}(g) = \frac{1}{2}\int_{t_0}^{t_f}\int_{\Omega_{\text{obs}}} \alpha_0 (p - p_a)^2 \, \mathrm{d}\boldsymbol{x} \, \mathrm{d}t \tag{7b}$$

$$J_{\text{reg}}(g) = \frac{1}{2}\int_{t_0}^{t_f}\int_{\Gamma_c} \left[\alpha_1 g_t^2 + \alpha_2 g^2 + \alpha_3 (\nabla g)^2 + \alpha_4 (\Delta g)^2\right] \mathrm{d}\Gamma \, \mathrm{d}t \tag{7c}$$

In Eqs. (7) $\alpha_0, \ldots, \alpha_4$ are positive weighting parameters. The first term is the square of the acoustic amplitude integrated over the observation region $\Omega_{\text{obs}}$ and time horizon $[t_0, t_f]$, where $p_a$ is the ambient, or the steady mean flow, pressure distribution. The term $J_{\text{reg}}(g)$ is a regularization term that enforces certain smoothness requirements on the controls. See Refs. 2 and 7 for more details. The set $\mathcal{G}_{\text{ad}}$ of admissible controls enforces the conditions $g(t, \boldsymbol{x}) = \nabla g(t, \boldsymbol{x}) = 0$ for $t \in (t_0, t_f)$ and $\boldsymbol{x} \in \partial\Gamma_c$, as well as $g(t_0, \boldsymbol{x}) = 0$, $\boldsymbol{x} \in \Gamma_c$. The first two conditions ensure that the control goes smoothly to zero at the endpoints of the controlled boundary, that is, at $\partial\Gamma_c$. The third condition enforces compatibility between the initial velocity field and boundary data.

**Adjoint Equations**

We use a gradient-based optimization procedure to solve the optimal control problem. The gradient is computed with the adjoint method. This approach is widely used, and a Refs. 2, 3, 8–14 represent a small sample of the work on adjoint methods for the optimization of unsteady flows. References 15–19 are a few of the many papers discussing adjoint equations for the optimization of steady Euler equations, mostly in the context of optimal design. However, our work here differs in two aspects from the cited literature. First, the governing flow equations, especially the boundary conditions, are different. Therefore, our adjoint PDEs, in particular, our adjoint boundary conditions, are different. Second, to gain more insight into the mathematical formulation of our problem, we use the optimize-then-discretize approach. This means that we derive the adjoint equations on the PDE level and then discretize our adjoint PDEs to obtain gradient information for the optimization algorithms. The gradient information obtained from this procedure is different than the one obtained by application of the adjoint equation procedure to the discretized version of the optimal control problem (3) and (6). Although the two outlined procedures do result in different gradient information, one expects, or at least hopes, that the error between the gradients computed by both approaches goes to zero if the discretization is refined. Of course, for this to happen, the optimal control problem and the adjoint PDEs must be formulated properly, and the discretization of the optimal control problem, as well as of the adjoint PDEs, must be suitable for the optimal control context. For our problem, and even much simpler optimal problems, these are nontrivial issues. Use of the optimize-then-discretize approach and the gradient checks, reported on in the section "Numerical Results," indicate that our approach is sensible.

In this paper, we focus on the aspects of the adjoint equation method that are different in our case from the approaches in the literature. The adjoint equations including boundary conditions are summarized later. Details on their derivation, as well as the computation of the objective function gradient, may be found in the Appendix. Our discretization of the optimal control problem, as well as the adjoint equations, is discussed in the next section.

The adjoint variables $\boldsymbol{\lambda} = (\lambda_1, \lambda_2, \lambda_3, \lambda_4)^T$ to the flow equations (3a) satisfy the differential equation

$$\boldsymbol{M}^T\boldsymbol{\lambda}_t + \sum_i \boldsymbol{A}^{i\,T}\boldsymbol{\lambda}_{x_i} = \boldsymbol{r} \tag{8}$$

where $\boldsymbol{M} = \boldsymbol{q}_u(\boldsymbol{u})$ and $\boldsymbol{A}^i = \boldsymbol{F}^i_u(\boldsymbol{u})$. The source term $\boldsymbol{r}$ in Eq. (8) is obtained by differentiating the right-hand side in Eq. (7b) with respect to the primitive variables. It is given by

$$\boldsymbol{r} = \alpha_0 \frac{p - p_a}{\gamma M^2} \begin{pmatrix} T \\ 0 \\ 0 \\ \rho \end{pmatrix} \chi_{\Omega_{\text{obs}}} \tag{9}$$

where $\chi_{\Omega_{\text{obs}}}$ is the indicator function, that is, $\chi_{\Omega_{\text{obs}}}(\boldsymbol{x}) = 1$ for $\boldsymbol{x} \in \Omega_{\text{obs}}$, and $\chi_{\Omega_{\text{obs}}}(\boldsymbol{x}) = 0$ otherwise. The final time condition for the adjoint variables is given by

$$\boldsymbol{\lambda}(t_f, \boldsymbol{x}) = 0 \tag{10}$$

In the Appendix, the adjoint boundary conditions are written in a compact form in terms of the adjoint characteristic variables. In the following, however, the adjoint boundary conditions are stated in terms of the adjoint variables $\boldsymbol{\lambda}$ for sake of completeness. We also define the adjoint momentum as $\boldsymbol{\mu} = (\lambda_2, \lambda_3)^T$. For suction ($g = \boldsymbol{v}^T\boldsymbol{n} \geq 0$), we obtain the three boundary conditions

$$g\left[\lambda_1 + \boldsymbol{v}^T\boldsymbol{\mu} + (\boldsymbol{v}^T\boldsymbol{v}/2)\lambda_4\right] = 0 \tag{11a}$$

$$\boldsymbol{\mu}^T\boldsymbol{n} + [\gamma/(\gamma-1)]g\lambda_4 = 0 \tag{11b}$$

$$g\left(\boldsymbol{\mu}^T\boldsymbol{s} + \boldsymbol{v}^T\boldsymbol{s}\lambda_4\right) = 0 \tag{11c}$$

The solid surface is a special case of suction with $g = 0$. Note from Eqs. (11) that only one boundary condition,

$$\boldsymbol{\mu}^T \boldsymbol{n} = 0 \tag{12}$$

is required. For blowing ($g = \boldsymbol{v}^T \boldsymbol{n} < 0$), we obtain two boundary conditions,

$$g\left(\boldsymbol{\mu}^T \boldsymbol{s} + \boldsymbol{v}^T \boldsymbol{s} \lambda_4\right) = 0 \tag{13a}$$

$$\boldsymbol{\mu}^T \boldsymbol{n} + [\gamma/(\gamma - 1)] g \lambda_4 + (M^2/T) g \left[\lambda_1 + \boldsymbol{v}^T \boldsymbol{\mu} + (\boldsymbol{v}^T \boldsymbol{v}/2)\lambda_4\right] = 0 \tag{13b}$$

Looking at the characteristics of the adjoint equation (8), one would expect only one boundary condition in the case $g = \boldsymbol{v}^T \boldsymbol{n} < 0$. A full analysis of these adjoint boundary conditions is in progress. However, note that the derived boundary conditions for suction and blowing are compatible as $g \to 0$.

## Implementation

In this section, we focus on the discretization scheme and the implementation of the transpiration boundary condition for the state equations.

### Discretization

Numerical simulation of aeroacoustic phenomena demands high numerical accuracy, that is, low dissipation and dispersion, to resolve convective flow features accurately over a wide range of space/timescales and amplitudes. To meet this need, most earlier approaches have utilized high-order accurate finite difference methods such as compact schemes[20] and the dispersion relation preserving methods.[21] Our study focuses on the application of optimal control to aeroacoustic problems, and, for this purpose, we have initially chosen to use the sixth-order central finite difference method with explicit high-wave-number damping and simple boundary treatments. This combination possesses excellent dispersion relation preserving properties (see, for example, Ref. 22). Its simplicity allows us to explore the issues involved in applying optimal control theory to aeroacoustic flows while avoiding complications that may arise due to more complex discretizations.

With this background, our Euler flow solver is based on a conservative extension of the explicit finite difference method described in Ref. 22. The Euler equations are formulated in a generalized coordinate system where the physical domain is mapped to a computational space: a unit square divided into an equally spaced grid system. This transformation allows clustering of grid points in regions of high gradients, simplifies the implementation of the boundary conditions, and allows the code to be used for moderately complex geometries. Although the code supports optimized finite differences with up to seven point stencils, for this study, spatial derivatives are approximated using standard sixth-order-accurate central differences in the interior, with third-order biased and one-sided differences used at boundaries that are designed to enhance stability when used with explicit time-advancement methods.[23] To suppress the growth of high-wave-number error modes, a fourth-order artificial dissipation term is added to the right-hand side of the discretized equations. This dissipation term is computed using fourth-order-accurate finite differences, and the dissipation parameter is chosen to damp out the error modes while avoiding excessive dissipation in the resolved scales, as established through numerical experimentation. Sponge terms[22,24] are used in the vicinity of the far-field boundary with a one–dimensional Riemann invariant treatment at the far-field boundary.

### Implementation of Boundary Conditions

As discussed earlier, the state boundary conditions (4) and (5) do not provide enough information to populate $\boldsymbol{u}$ on the boundary. For subsonic suction, the physical boundary condition (4) has to be augmented by three numerical boundary conditions. For subsonic blowing, one numerical boundary condition is needed in addition to the three physical boundary conditions (5). Analogous considerations apply to the adjoint PDE. However, because the adjoint PDEs are solved backward in time, characteristics that are outgoing for the state equation are incoming for the adjoint equations and vice versa. The following describes our implementation of state and adjoint boundary conditions.

#### *Implementation of Wall Transpiration Boundary Conditions*

Most wall boundary condition treatments in the literature focus on solid walls and the numerical implementation of the no-penetration boundary condition. In the course of our study, we tried to modify several existing boundary condition treatments to accommodate wall normal suction and blowing. First, we tried the common treatment of solving the continuity equation for density on the boundary, imposing the normal velocity actuation, as well as extrapolation of the remaining state variables from the inner domain. This treatment produces considerable numerical noise that corrupts the dilatation and vorticity fields and severely reduces the allowable time step for a stable solution. Next, we tried the one-dimensional characteristic-based approaches of Thompson,[25,26] Poinsot and Lele,[27] and Giles.[28] We could not successfully modify any of these methods to actuate a time- and space-varying suction and blowing control without eventual blow-up of the simulation.

We eventually arrived at an implementation with acceptable accuracy and stability properties that is based on the approach originally formulated by Sesterhenn,[1] who expresses the inviscid part of the equations as a decomposition into several plane waves aligned with the numerical grid. This is done in an attempt to merge finite differencing with schemes based on compatibility equations such as Moretti's $\lambda$ scheme.[29] In this approach, transport equations are written for pressure, normal, and tangential velocities in terms of the pseudoacoustic wave amplitudes. These pseudowaves may not have any physical significance in two- or three-dimensional flows, but, in one dimension, they coincide with the temporal change of acoustic wave amplitudes closely related with the Riemann invariants of homentropic flows. Also, the introduction of these pseudowaves allows a more direct and natural implementation of wall boundary conditions as opposed to the locally one-dimensional inviscid approximation of Poinsot and Lele.[27] We use Sesterhenn's decomposition only on the wall boundary to implement the transpiration boundary conditions (4) and (5). In the following, body coordinates $\boldsymbol{s}$–$\boldsymbol{n}$ are used, where $\boldsymbol{n}$ denotes the outward normal direction to the boundary and $\boldsymbol{s} = (s_1, s_2)^T = (-n_2, n_1)^T$ is the unit tangential vector. We define the following "pseudowaves" in the tangential and normal directions:

$$X_s^{\pm} = (\boldsymbol{v}^T \boldsymbol{s} \pm c)\left[(1/\rho c)\partial_s p \pm \partial_s \boldsymbol{v}^T \boldsymbol{s}\right] \tag{14a}$$

$$X_n^{\pm} = (\boldsymbol{v}^T \boldsymbol{n} \pm c)\left[(1/\rho c)\partial_n p \pm \partial_n \boldsymbol{v}^T \boldsymbol{n}\right] \tag{14b}$$

Transport equations for the velocity components and pressure can be recast in terms of these pseudowaves as

$$\partial_t \boldsymbol{v}^T \boldsymbol{n} = -\tfrac{1}{2}\left(X_n^+ - X_n^-\right) - \boldsymbol{v}^T \boldsymbol{s} \partial_s \boldsymbol{v}^T \boldsymbol{n} - (\boldsymbol{v}^T \boldsymbol{s})^2/R \tag{15a}$$

$$\partial_t \boldsymbol{v}^T \boldsymbol{s} = -\tfrac{1}{2}\left(X_s^+ - X_s^-\right) - \boldsymbol{v}^T \boldsymbol{n} \partial_n \boldsymbol{v}^T \boldsymbol{s} + \boldsymbol{v}^T \boldsymbol{s} \boldsymbol{v}^T \boldsymbol{n}/R \tag{15b}$$

$$\partial_t p = -(\rho c/2)\left(X_s^+ + X_s^- + X_n^+ + X_n^-\right) + \rho c^2 \boldsymbol{v}^T \boldsymbol{n}/R \tag{15c}$$

At boundary points, $X_s^{\pm}$ are determined from the boundary data available at the current time. However, in the $\boldsymbol{n}$ direction, the Mach number $M_n = \boldsymbol{v}^T \boldsymbol{n}/c$ determines where the $X_n$ pseudowaves originate. For example, when the flow is locally subsonic, $X_n^-$ enters the domain from outside, whereas $X_n^+$ leaves the domain (Fig. 1). Waves that enter the domain are specified so that the imposed physical boundary conditions are satisfied. As mentioned earlier, one physical boundary condition, $\boldsymbol{v}^T \boldsymbol{n} = g$, must be imposed on the boundary for subsonic suction. The unknown pseudowave $X_n^-$ is determined from Eq. (15a):

$$X_n^- = X_n^+ + 2\left[\partial_t g + \boldsymbol{v}^T \boldsymbol{s} \partial_s g + (\boldsymbol{v}^T \boldsymbol{s})^2/R\right] \tag{16}$$

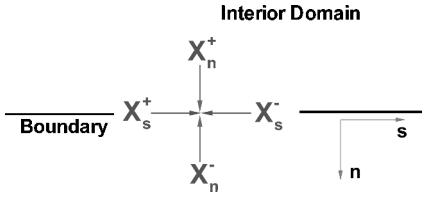


**Fig. 1 Pseudowaves at a subsonic boundary point.**

The time derivative of pressure can now be computed by substitution for $X_n^-$ from Eq. (16) in Eq. (15c). The energy equation can be written in terms of entropy as

$$\partial_t S + v^T s \partial_s S + v^T n \partial_n S = 0 \tag{17}$$

where $\partial_n S$ is computed from the interior domain with a one-sided finite difference stencil, allowing us to compute the time derivative of entropy from Eq. (17). Similarly, if $\partial_n v^T s$ is computed by a one-sided finite difference stencil, the time derivative of $v^T s$ can also be computed from Eq. (15b). Now, we have $\partial_t v^T s$, $\partial_t v^T n$, $\partial_t p$, and $\partial_t S$ at our disposal, and we can easily compute the temporal derivative of any other flow quantity. For instance, to compute $\partial_t \rho$, one can use the Gibbs equation

$$\mathrm{d}h = T\,\mathrm{d}S + \frac{\mathrm{d}p}{\rho} \tag{18}$$

in conjunction with the equation of state (1), to write the density time derivative in terms of entropy and pressure.

For subsonic blowing, however, three physical boundary conditions must be imposed, $v^T n = -g$, $S = 0$, and $\omega = 0$. Again, the unknown pseudowave is determined from Eq. (16), and the pressure time derivative is subsequently computed from Eq. (15c). The time derivative of density is found by enforcement of a zero rate of change in entropy in Eq. (18):

$$\partial_t \rho = (1/c^2)\partial_t p \tag{19}$$

Vorticity $\omega$ is given by

$$\omega = -\partial_s v^T n + \partial_n v^T s - (v^T s/R) \tag{20}$$

where $\partial_s v^T n = \partial_s g$ is a known quantity. The boundary condition $\omega = 0$ is enforced weakly by substitution of $\partial_n v^T s = \partial_s v^T n + v^T s/R$ in the right-hand side of Eq. (15b).

*Implementation of Adjoint Boundary Conditions*

Our treatment of the adjoint boundary conditions differs from that of the state boundary conditions just described. Although we could have applied a boundary treatment similar to that used for the state, our adjoint boundary condition implementation is instead based on simple extrapolation of appropriate adjoint characteristic quantities, similar to that described for the Euler equations in Ref. 30. This simple implementation has been sufficient for all of the adjoint computations presented here. We point out that the optimize-then-discretize framework allows us to use different implementations in the state and adjoint discretizations and that we have made use of that flexibility here.

There exist nonsingular matrices $P$, $L$, and a diagonal matrix $\Lambda$ with entries $v^T n$, $v^T n$, $v^T n + c$, and $v^T n - c$, such that

$$\sum_i n_i A^{i\,T} = L^{-T} \Lambda P^T$$

(For details, see the Appendix.) Because the adjoint equations are solved backward in time, a negative eigenvalue $v^T n$, $v^T n \pm c$ indicates flow of information from the inner domain toward the boundary. To populate the adjoint vector on the boundary, numerical boundary conditions are needed to complement the derived adjoint boundary conditions. In this work, we simply extrapolate the components of $\Psi = (\Psi_1, \Psi_2, \Psi_3, \Psi_4)^T \overset{\text{def}}{=} P^T \lambda$ that correspond to negative propagation speeds in the direction normal to the boundary.

For subsonic suction, a third-order extrapolation of $\Psi_4$ from the inner domain provides the numerical boundary condition that complements the adjoint boundary conditions (11), or their equivalent expression (33–35) in terms of the characteristic adjoint variables.

For subsonic blowing, we extrapolate $\Psi_1$ and $\Psi_4$, whereas $\Psi_2$ and $\Psi_3$ are determined from the adjoint boundary conditions (13) or, more precisely, their equivalent expression (35) and (39) in terms of the characteristic adjoint variables derived in the Appendix.

**Far-Field Sponge Treatment for the State and Adjoint Equations**

We use sponges at the far-field boundaries to prevent outgoing acoustic and numerical waves from being reflected in the domain. A sponge is applied by addition of a source term of the form $-\theta(x)(q - \hat{q})$ to the Euler equations in the sponge region. The function $\theta(x)$ is a strictly increasing function that is only nonzero in the sponge and varies from zero at the inner edge to a large value at the outer edge. The state solution is forced to approach the prescribed field $\hat{q}$ in the sponge region. Note that the adjoint of the sponge is of the form $\theta(x) M^T \lambda$, which is added to the right-hand side of Eq. (8). This sponge term forces the adjoint variable $\lambda$ effectively to vanish in the sponge region.

## Numerical Results

In our model problems, $\Omega = \{x \in \mathbb{R}^2 : x_2 > 0\}$, $\Gamma_c = \{x \in \mathbb{R}^2 : x_2 = 0, a \le x_1 \le b\}$, and $n = (0, -1)^T$.

**Test Case 1**

In this section, we present optimal control results for the test problem depicted in Fig. 2. In the following, the source period $T_p$ and the wavelength $L$ are used for nondimensionalization A time-harmonic line source is located at a distance $H = 5$ from a solid wall. The computational domain is $\Omega = [-3.5, 3.5] \times [0, 7]$, with periodic boundary conditions in the horizontal direction and a sponge-type nonreflecting far-field boundary condition applied at the top boundary. The control objective is Eqs. (7), with observation region $\Omega_{\text{obs}} = [-2, 2] \times [\frac{1}{2}, \frac{3}{2}]$ (the rectangular box shown in each of the contour plots of Figs. 3 and 4b). The time interval is from $t_0 = 30$ to $t_f = 50$. Because the pressure fluctuations are usually very small, the weight $\alpha_0$ in the control objective (7) is chosen to be large relative to the other weights. We use $\alpha_0 = 10^6$, $\alpha_1 = 10^{-3}$, $\alpha_2 = 10^{-7}$, and $\alpha_3 = \alpha_4 = 10^{-3}$. The selection of weights is an important engineering design question. When optimal control problems are solved for specific applications, a more systematic way to determine their influence on the controlled flow is desirable. However, for the test cases presented here, we have selected the weights based on experience in Ref. 2, as well as experimentation in the context of the present test problems.

Wall normal transpiration constitutes the boundary control, defined over $[-3, 3] \times [t_0, t_f]$. The time interval comprises 800 uniform time steps of size $\Delta t = 0.025$, and the spatial mesh (141 × 141)

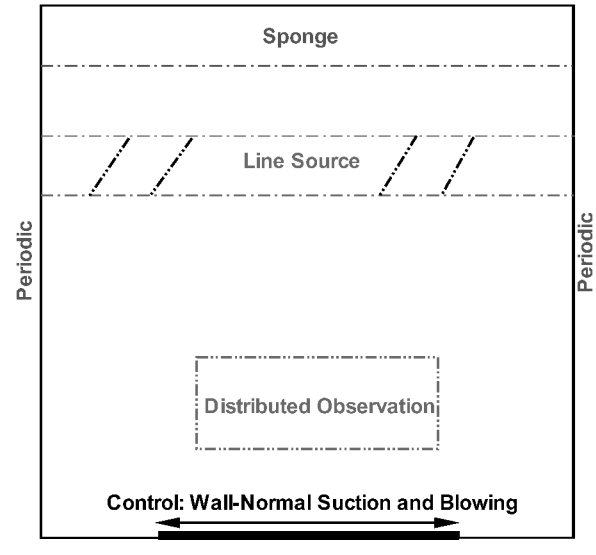


**Fig. 2 Schematic of test case 1.**

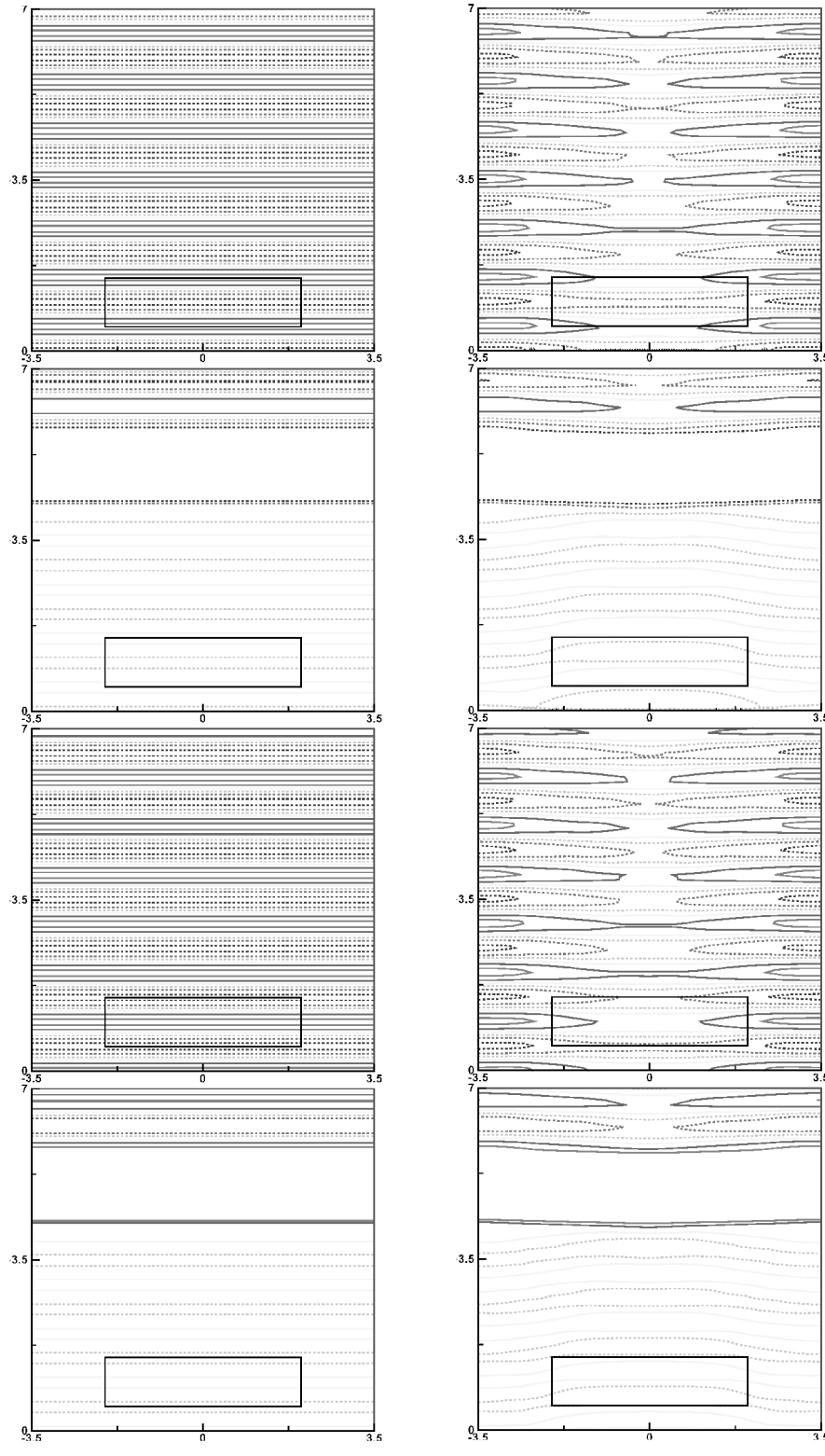

a) No control b) Optimal control

**Fig. 3 Contours of $p - p_a$ at four equally spaced instants, spanning one period of oscillation $T_p$ (six equally spaced contour levels between $\pm 7.0 \times 10^{-6}$).**

has uniform spacing of $\Delta x_1 = \Delta x_2 = 0.05$. Because the line source is harmonic, and the effect of nonlinearities away from the source region is negligible, the flowfield exhibits a limit-cycle behavior with period $T_p$ as $t \to \infty$. The initial time $t_0$ is chosen large enough for this limit-cycle pattern to be established effectively in the domain. Figure 3a shows contours of pressure fluctuations about the ambient pressure, $p - p_a$, for the uncontrolled flow within one period of oscillation.

The analytical solution for the infinite-dimensional no-control problem can be found easily by superimposition of an image line source at $x_2 = -H$. The second component of velocity $v_2$ and pressure $p$ can be written as

$$v_2 = 4v_m \sin(2\pi x_2) \cos\left[2\pi\left(H - t + \tfrac{1}{4}\right)\right] \tag{21a}$$

$$p = 4p_m \cos(2\pi x_2) \cos[2\pi(H - t)] \tag{21b}$$

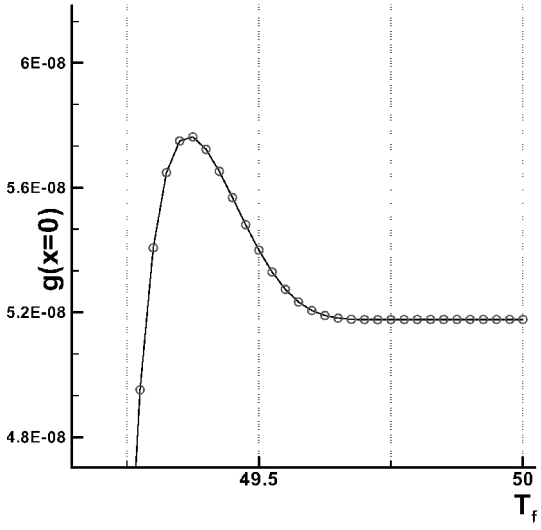


a) Control $g$ near the final time $t_f$

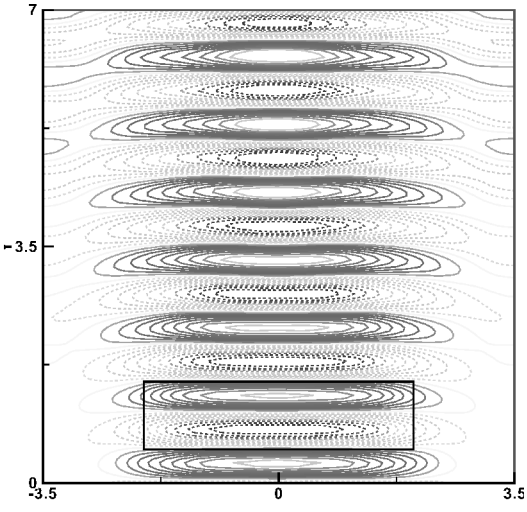


b) At time $t = 40.5$, $p_{\text{optimal}} - p_{\text{nocontrol}}$ (20 evenly spaced contours between $\pm 3.5 \times 10^{-6}$)

**Fig. 4 Effect of control for case 1.**

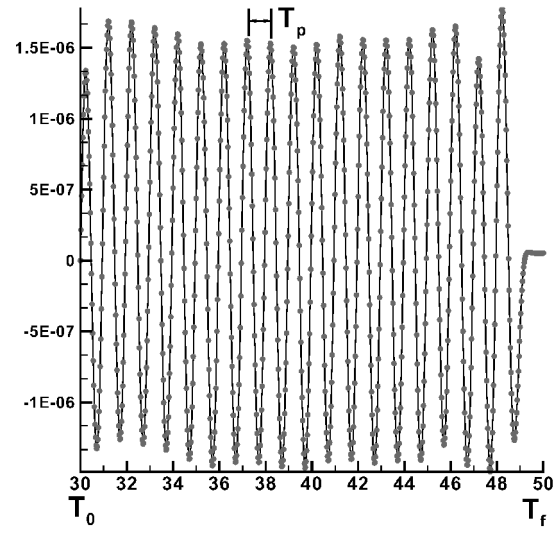


a) $x = 0$

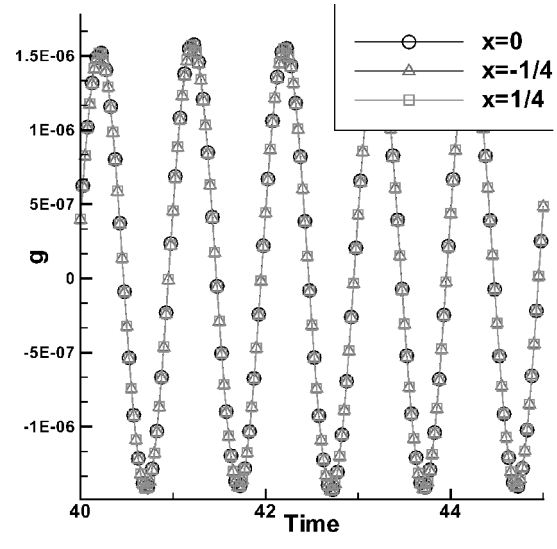


b) $x = 0, \pm 1/4$

**Fig. 5 Time history of control $g$.**

In Eqs. (21), the velocity and pressure amplitude of the harmonic line source are denoted by $v_m$ and $p_m$, respectively. Equation (21a) satisfies the inviscid wall boundary condition at $x_2 = 0$ at all times. Further examination of Eq. (21b) shows that, for $t = H/c + (2n+1)/4$, $n = 0, 1, 2, 3, \ldots$, the pressure fluctuation vanishes everywhere in the domain. This behavior is seen in the second and fourth plots of Fig. 3a.

For this test case, the value of the objective function (7) at the initial iterate $g_0 = 0$ (no control) is $J(g_0) = J_{\text{obs}}(g_0) = 1.2 \times 10^{-3}$. After 15 nonlinear conjugate gradient iterations,[2] the computed control $g_{15}$ reduces the observation term in the objective function to $J_{\text{obs}}(g_{15}) = 6.6 \times 10^{-4}$, which is about 45% of its initial value. Because of our choice of weights $\alpha_i$, we obtain that $J_{\text{reg}}(g_{15}) \approx 10^{-10} J_{\text{obs}}(g_{15})$, that is, the value $J(g_{15})$ of the objective function (7) can be equated with $J_{\text{obs}}(g_{15})$. The same is also true for the other test cases. The acoustic pressure contours for the controlled run are shown in Fig. 3b. To analyze the behavior of the computed control, the time history of the control at $x_1 = 0, \pm\frac{1}{4}$ is plotted in Fig. 5. Figure 5a depicts the time history of control at $x_1 = 0$. Note that the control has no difficulty in picking up the source frequency, and the control oscillates with an approximately constant amplitude for most of the time window $(t_0, t_f)$. Close to the final time, the control loses the harmonic behavior and becomes approximately constant. Figure 5b shows the time history of control at three locations on the wall, $x_1 = 0, \pm\frac{1}{4}$, separated by one-quarter wavelength. Figure 5b demonstrates that the controls at these three locations are exactly in phase. Further checks reveal that the control indeed is constant across the control region and is only a function of time. Because the lower edge of the observation region is located at a distance $\frac{1}{2}$ above the wall, it takes about $\frac{1}{2}$ time units for the effect of the boundary actuation to be felt in the observation region, explaining the behavior of the control near the final time shown in Fig. 4a. From $t = 49.5$ onward, the control cannot affect the observation term, and, hence, it tries to minimize the contribution of the regularization term. The contribution of the spatial derivatives $g_{x_1}$ and $g_{x_1x_1}$ to Eqs. (7) is zero, and the contribution of the time regularization term $\|g_t\|_2^2$ is approximately $4\pi^2 \approx 39.5$ times larger than the regularization term $\|g\|_2^2$ for a simple harmonic oscillation. Therefore, the main focus of the optimal control in the time period $(39.5, t_f)$ is to reduce $g_t$ initially, which is clearly achieved by creating a plateau near the final time $t_f$. To understand the effect of the computed control, one can subtract the uncontrolled pressure field from the optimal control pressure field as shown in Fig. 4b. Because the amplitude of flow quantities are small, the nonlinear terms in the governing equations are negligible and the contour plot of Fig. 4b isolates the effect of boundary actuation. Note that the boundary control creates a nearly planar wave to counter the wave system (21) in the observation region. A perfect cancellation is not possible because the wave produced by the control cannot cancel the wave system (21) at all times. The optimal control targets instants of time at which the observation region has high-amplitude waves (the first and third snapshots of Fig. 3a) and tries to reduce

these waves by producing the wave shown in Fig. 4b. The control slightly disturbs the approximately silent instants observed in the second and fourth plots of Fig. 3b.

**Test Case 2**

In this test case, we control the scattered and refracted wave pattern arising from the interaction of a monopole sound source with an inviscid vortex. Again, all flow quantities are nondimensionalized with source period $T_p$ and acoustic wavelength $L$. The monopole sound source, modeled as a source term in the energy equation, is located at (0, 5) and interacts with an inviscid vortex[31] of circulation $2\pi/5$ (counterclockwise) and radius $\frac{1}{2}$ located at (0, 3.5). The computational domain, control objective, and the spatial and temporal discretizations are identical to that of test case 1. Sponge-type nonreflecting far-field boundary conditions are now used on the left, right, and top boundaries. The distance between the vortex and the

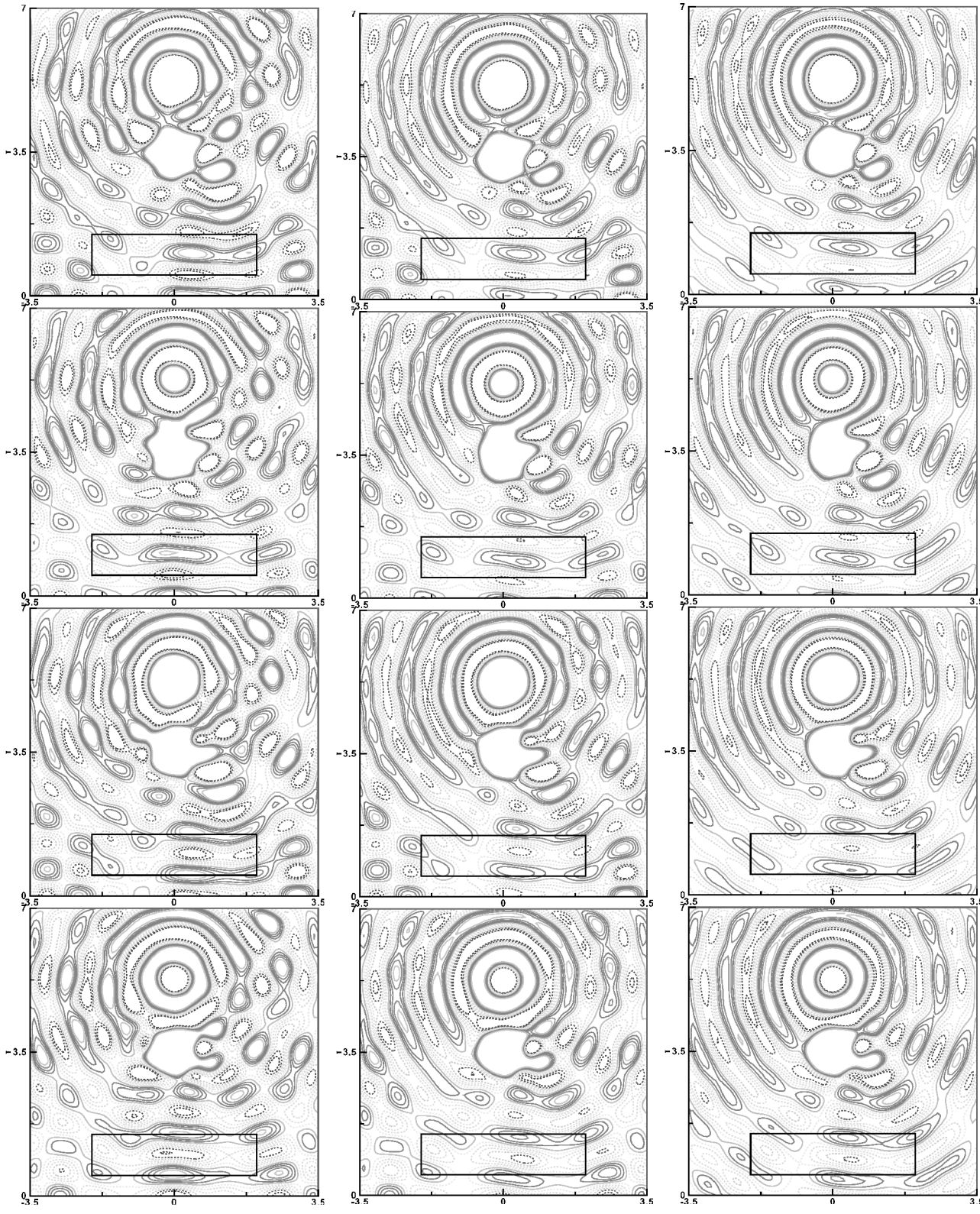

**a) No control** **b) Optimal control** **c) Far-field BC on bottom boundary**

**Fig. 6 Contours of $p - p_a$ at four equally spaced instants, spanning one period of motion $T_p$ (six contour levels between $\pm 1.75 \times 10^{-4}$).**

solid wall is large enough to ignore the effect of the image vortex in the optimization time interval comfortably. Hence, the vortex is considered to be stationary and the mean flow pressure distribution to be steady. The time interval comprises 600 uniform time steps of size $\Delta t = 0.025$ from time $t_0 = 30$ to time $t_f = 45$. Again, the initial time is larger than the time required for the limit-cycle pattern to be established effectively in the domain.

After 20 optimization iterations, the control objective is reduced from $J_{\text{obs}}(g_0) = 0.49$ to $J_{\text{obs}}(g_{20}) = 0.34$. The acoustic pressure contours for the no-control and optimal-control simulations are shown in Figs. 6a and 6b, respectively. In the no-control simulation, the scattered wave behind the vortex is mostly observed in the right half of the observation region, which is due to the counterclockwise circulation of the vortex. The left half is relatively silent. The solid wall intensifies the incident waves and forces the waves to move horizontally.

However, focus shifted onto the observation region of the optimal control run reveals that the main difference between the two runs is the slanted contours of the optimal control simulation. To understand the control mechanism, another simulation is performed where the solid wall is replaced with a nonreflecting boundary condition based on Riemann extrapolation. Figure 6c shows four snapshots of the acoustic pressure field at the same instants in time by the use of the Reimann boundary treatment. The pressure contours in the observation region for this run are very similar to that of the optimal control run, both slanting at an angle to the horizon, unlike the almost flat contours of the uncontrolled run. This suggests that the optimal control attempts to mimic an absorbing boundary. The computed optimal control makes the wall nearly transparent to the incident waves, thereby preventing them from reflecting and intensifying the sound measured in the observation region.

In the no-control run, the refracted/reflected wave pattern seen in the middle of the observation region is approximately horizontal. However, the wave system produced by the boundary actuation (Fig. 7b) and the wave pattern observed in the center of the optimal control plots (Fig. 6) slant in opposite directions. The production of the slanted wave of Fig. 7b by the boundary actuation is further validated by Fig. 7a, where the time history of control at three positions, $x_1 = -0.25, 0$, and $0.25$, separated by one-quarter acoustic wavelength, is plotted. The phase difference in control actuation at these three locations allows for the production of waves with slanted fronts. Note that the control amplitude is smaller at $x_1 = -0.25$ than at the other two locations. This shows that the optimal control avoids disturbing the relatively silent left half of the observation region while attenuating the noisy right half of this region.

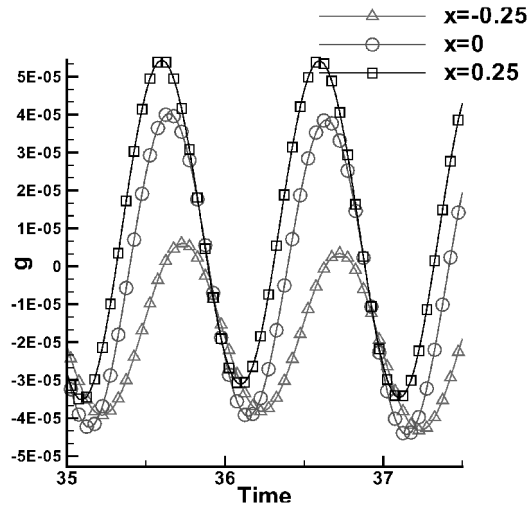


**a) Time history of control $g$ at $x_1 = 0, \pm\frac{1}{4}$**

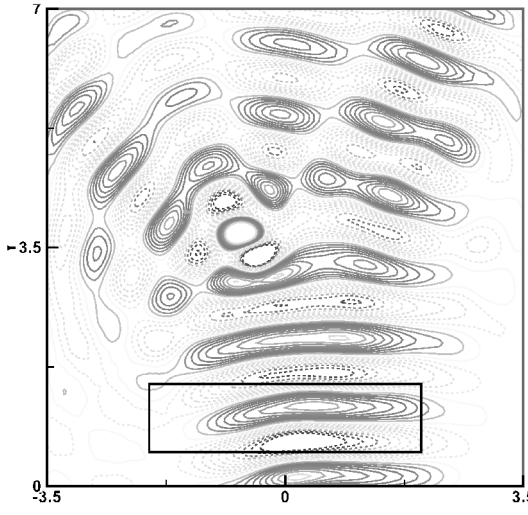


**b) At time 40.75, $p_{\text{optimal}} - p_{\text{nocontrol}}$ (20 contours between $\pm 9.0 \times 10^{-5}$)**

**Fig. 7 Effect of control for case 2.**

**Test Case 3**

In test case 2, we argued that the computed transpiration boundary actuation effectively rendered the controlled surface transparent to incident waves. Test case 3 allows us to quantify how closely a transpiration wall is capable of mimicking a nonreflecting boundary condition. The computational domain is $\Omega = [-12, 12] \times [0, 14]$, with periodic boundary conditions enforced in the horizontal direction and a sponge nonreflecting boundary treatment in the vicinity of the top boundary. The control objective is identical in form to that of the preceding test cases and is defined over $\Omega_{\text{obs}} = [-5, 5] \times [5, 9]$ and time horizon $[2, 9]$, comprising 175 uniform time steps $\Delta t = 0.04$. The spatial mesh ($241 \times 141$) has uniform spacing $\Delta x_1 = \Delta x_2 = 0.1$ in both directions and transpiration control is allowed over the entire bottom boundary. The initial condition is a Gaussian acoustic pulse of amplitude $\epsilon = 10^{-3}$, with standard deviation $\sigma = 0.25$, centered at mean height $x_2^* = 8$ above the wall:

$$v_1 = 0, \qquad v_2 = -(\epsilon/2)\exp\left\{-\tfrac{1}{2}\left[\left(x_2 - x_2^*\right)/\sigma\right]^2\right\}$$

$$p - p_a = -\rho_a c_a v_2, \qquad \rho - \rho_a = (p - p_a)/c_a^2 \tag{22}$$

In Eqs. (22), the subscript $a$ denotes the ambient condition assumed to be a uniform quiescent flow where $\rho_a = T_a = 1$ and $c_a = 2$. The acoustic pulse propagates at the ambient speed of sound $c_a = 2$ toward the wall, and, at $t_0$, the beginning of the optimization horizon, it is located at $x_2 = 4$. For the no-control simulation, the pulse reflects off of the solid wall, passes through $\Omega_{\text{obs}}$, and reaches $x_2 = 10$ at the final time $t_f$. We use $\alpha_0 = 10^6$, $\alpha_1 = 10^{-3}$, $\alpha_2 = 10^{-4}$, and $\alpha_3 = \alpha_4 = 10^{-3}$. Optimization starts at the no-control configuration with $J(g_0) = J_{\text{obs}}(g_0) = 9.19 \times 10^{-1}$, $\|\nabla J(g_0)\|_{\mathcal{G}} = 3430$ and is terminated after 133 nonlinear conjugate gradient iterations $J_{\text{obs}}(g_{133}) = 3.98 \times 10^{-5}$, $\|\nabla J(g_{133})\|_{\mathcal{G}} = 2.59$. The norm, $\|g\|_{\mathcal{G}}$, which is specified in Ref. 2, is related to

$$\int_{t_0}^{t_f}\int_{\Gamma_c} g^2 + g_t^2 + |\nabla g|^2 + |\Delta g|^2 \, \mathrm{d}\Gamma \, \mathrm{d}t$$

and is not the Euclidean norm. Four snapshots of the acoustic pressure contours of the no-control and optimally controlled flow are shown in Fig. 8. We note that, whereas the uncontrolled flow is one dimensional, the controlled flow is two-dimensional due to the finite sized control region on the bottom wall.

Figure 8a shows that the observation region is quiet except for the time interval in which the reflection off of the solid wall passes through it. Therefore, the optimal control actuation can not decrease the objective function unless it eliminates the reflection from the wall and makes the controlled wall transparent to the incident acoustic pulse. This behavior is evident in Fig. 8b, where the

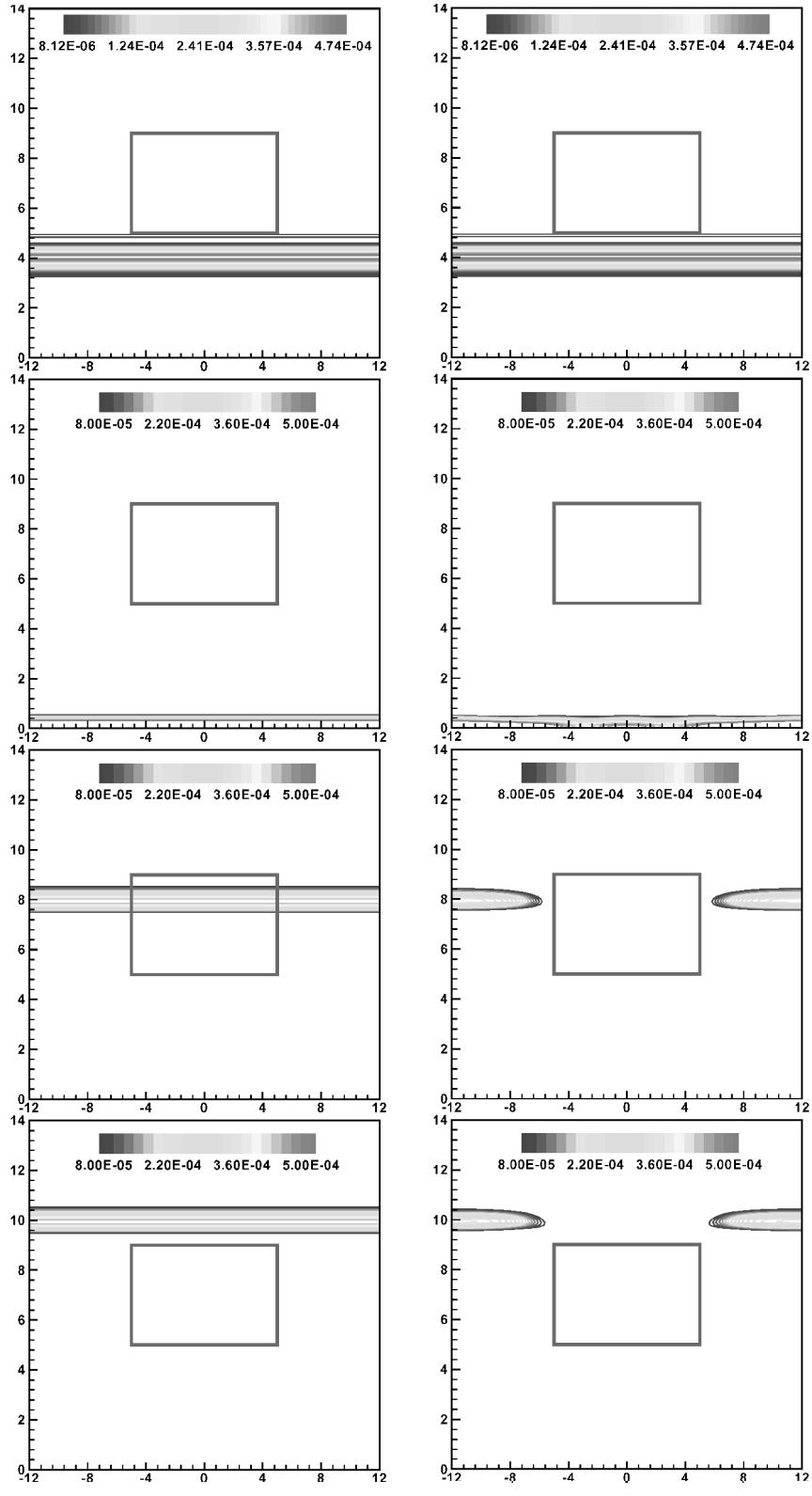


**a) No control** **b) Optimal control**

**Fig. 8 Contours of $p - p_a$ at instants $t = 2, 4, 8$, and 9 (41 contour levels between $8.12 \times 10^{-6}$ and $4.74 \times 10^{-4}$).**

control actuation has allowed the central portion of the acoustic pulse between $[-5, 5]$ to pass through the wall without noticeable reflection.

To access the performance of the optimal control transpiration boundary condition (BC) in producing an essentially nonreflecting boundary condition, we remove the lower wall and enforce the well-known nonreflecting treatments: 1) Riemann extrapolation and 2) sponge. Then we compute

$$J_{\text{obs}} = \frac{1}{2}\int_{t_0}^{t_f}\int_{\Omega_{\text{obs}}} \alpha_0 (p - p_a)^2 \, d\boldsymbol{x}\, dt, \qquad \alpha_0 = 10^6$$

for each case, to estimate the amount of reflections produced by each boundary treatment. For the optimal transpiration boundary control, we find that $J_{\text{obs}} \approx 4 \times 10^{-5}$, Riemann extrapolation BCs give $J_{\text{obs}} \approx 6.4 \times 10^{-5}$, and sponge BCs lead to $J_{\text{obs}} \approx 1. \times 10^{-6}$.

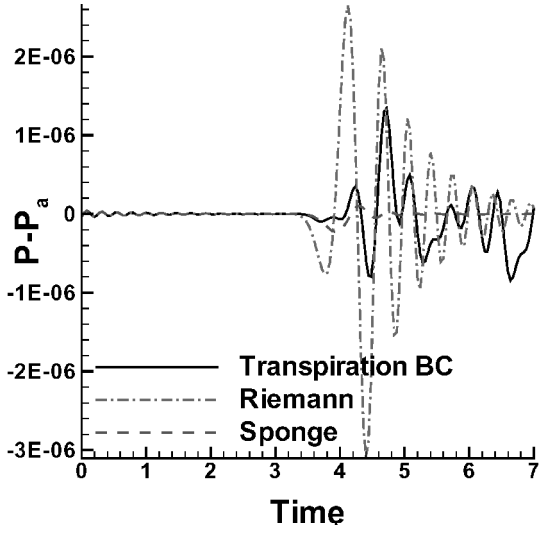


**Fig. 9 Time history of pressure fluctuations at (0, 7) for case 3.**

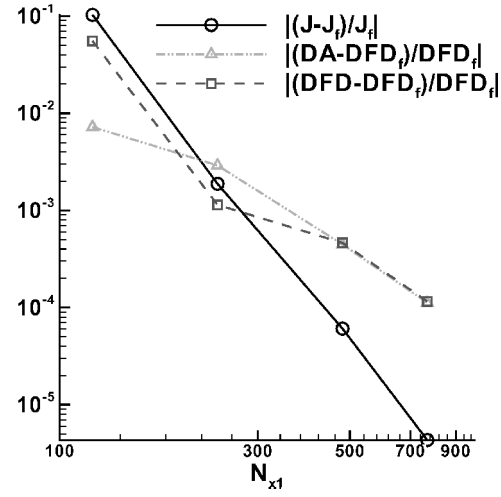


**Fig. 10 Mesh refinement study for test case 3, showing approximate directional derivative (DA) and the fourth-order finite difference approximation to the directional derivative (DFD).**

We note that the Riemann condition performs somewhat worse than the sponge because Riemann treatments are well known to reflect the nonsmooth, numerical error waves. The amount of reflections in the observation region for the controlled wall is less than the Riemann treatment, whereas it is considerably higher than the sponge treatment. Because the transpiration and Riemann BC implementations are both based on the flow characteristics, the Riemann BC is a reasonable reference against which the performance of the transpiration BC can be measured. That the optimal control boundary performs slight better than the Reimann BC is likely due to the numerical error associated with extrapolation in the Reimann BC. Figure 9 compares the amplitudes of the reflected waves by plotting the time history of pressure fluctuations in the center of the observation region. The maximum sound amplitude for the optimal control simulation is slightly less than one-half of the peak reflection amplitude due to the Riemann treatment, whereas the peak reflection amplitude of the sponge treatment is about an order of magnitude smaller than the other two.

### Gradient Accuracy

As we have mentioned earlier, we use the optimize-then-discretize approach to compute gradient information. That is, we first derive adjoint equations and the objective function gradient on the PDE level and then discretize the resulting expressions. We denote the result by $[\nabla J(g)]_h$ to indicate that discretization is performed after differentiation. The resulting derivative approximation differs from gradient $\nabla[J_h(g)]$. It is obtained by discretization of the optimal control problem and then computation of the gradient of the resulting finite dimensional objective function $J_h(g)$. If adjoint computations are performed correctly, and if discretizations of state equation, objective function, and adjoint equations are chosen properly, one would expect that $[\nabla J(g)]_h - \nabla[J_h(g)] \to 0$ as the discretization level $h$ is refined. Moreover, the rate with which $[\nabla J(g)]_h - \nabla[J_h(g)]$ goes to zero should be related to the approximation properties of the underlying discretization schemes. That, in fact, the convergence $[\nabla J(g)]_h - \nabla[J_h(g)] \to 0$ as $h \to 0$ is obtained is not at all straightforward. Even for optimal control problems far less complex than the one considered here, Refs. 32 and 33 offer some sobering results.

The results in this section provide evidence that in our treatment $[\nabla J(g)]_h - \nabla[J_h(g)] \to 0$ as the discretization level $h$ is refined. Because we do not have access to the gradient of the discretized objective function $J_h(g)$, we choose an arbitrary unit direction $\delta g$ in the space of admissible controls and compare $\langle [\nabla J(g)]_h, \delta g \rangle_{\mathcal{G}}$ with a finite difference approximation of $\langle \nabla[J_h(g)], \delta g \rangle_{\mathcal{G}}$. Here, $\langle g_1, g_2 \rangle_{\mathcal{G}}$ is a weighted Euclidean norm corresponding to $\| \|_{\mathcal{G}}$, which is specified in detail in Ref. 2. To select a suitable finite difference step size $\epsilon$, we evaluate the discretized objective function at $\pm\epsilon\delta g$ and $\pm 2\epsilon\delta g$ and compare the second-order approximation $[J_h(g + \epsilon\delta g) - J_h(g - \epsilon\delta g)]/(2\epsilon)$ with a fourth-order finite difference approximation. The finite difference step size $\epsilon$ is varied until these two approximations agree to a relative error of less than $10^{-6}$ (for test case 3). For example, for test case 3, which uses a $241 \times 141$ grid and $g = 0$, the computed second-order approximation to $\langle \nabla[J_h(g)], \delta g \rangle_{\mathcal{G}}$ is $-535.1712$, and the computed fourth-order approximation is $-535.1714$. The corresponding directional derivative computed with the optimize-then-discretize approach is $\langle [\nabla J(g)]_h, \delta g \rangle_{\mathcal{G}} = -535.1872$.

Figure 10 shows the results of grid convergence studies with grids ranging in size from $241 \times 141$ to $961 \times 561$. For our computations, the solution at the finest discretization $961 \times 561$ is assumed to be the reference solution and is denoted by subscript $f$. In Fig. 10, three relative error measures have been plotted against the number of mesh points $N_{x_1}$, where $N_{x_1}$ is the number of grid points in the $x_1$ direction, and the number of grid points in the $x_2$ direction is $(7/12)(N_{x_1} - 1) + 1$, chosen to give the same grid spacing in both directions. In Fig. 10, $J$ denotes the value of the objective function (7a). The approximate directional derivative $\langle [\nabla J(g)]_h, \delta g \rangle_{\mathcal{G}}$ is obtained by discretization of the adjoint equations (optimize then discretize), and the fourth-order finite difference approximation to the directional derivative $\langle \nabla[J_h(g)], \delta g \rangle_{\mathcal{G}}$ is obtained by differentiation of the discretized objective function.

Both axes of Fig. 10 have a logarithmic scale, and the slope of each line measures the order of convergence as discretization is further refined. The observed rate of convergence for the objective function $J$ is approximately 5.5, whereas the relative errors between the directional derivative approximations converge with an observed rate of approximately three. Because we use a finite difference scheme that is sixth-order accurate in the interior and third-order accurate near the boundary, because we apply a fourth-order time-stepping scheme, and because we employ sponge and Riemann extrapolation at the far field, it is difficult to conjecture what theoretical convergence rates should be obtained. However, our observed convergence rates for the various quantities are sensible. In particular, the comparison between the derivative information $\langle [\nabla J(g)]_h, \delta g \rangle_{\mathcal{G}}$ obtained from our optimize-then-discretize approach and the finite difference approximation to the directional derivative $\langle \nabla[J_h(g)], \delta g \rangle_{\mathcal{G}}$ of the discretize-then-optimize approach support our procedure.

## Conclusions

This work focuses on several important issues encountered in the optimal boundary control of aeroacoustic flows governed by high-order central finite difference discretizations of the unsteady

Euler equations. These issues include: proper resolution of fluctuating flow quantities, nonreflecting far-field boundary treatments, and solid wall modeling. The importance of these issues is well known for computational aeroacoustics, but they are also critically important when optimal control is applied to aeroacoustic flows. In addition, optimal transpiration boundary control of aeroacoustics also requires the formulation and implementation of accurate near-field BCs on the controlled segment of the boundary. It is argued, based on the characteristic wave propagation speeds normal to the controlled boundary, that subsonic suction requires one physical BC, whereas blowing requires three physical BCs. Our implementation of the transpiration BC is based on a decomposition of the inviscid fluxes into several planar pseudowaves aligned with the boundary tangent and boundary normal directions by the use of a technique originally introduced by Sesterhenn.[1] The transpiration BC is applied to three optimal control test problems. A continuous adjoint gradient-based method is used to solve the optimization problems, and the adjoint equation, its end time condition, and BCs are stated and discussed. Despite the difference in the number of derived adjoint BCs for suction, blowing, and solid walls, the adjoint BCs are compatible because the control tends to zero. The first test problem demonstrates that the transpiration control actuation is capable of producing well-resolved acoustic waves that reduce the observed sound amplitude by means of wave cancellation. In the second test problem, the transpiration BC mimics a nonreflecting BC on the controlled surface to eliminate the intensifying effect of reflections off of the solid wall. The final test problem demonstrates that optimal transpiration control is capable of creating a nonreflecting surface that rivals the widely used Riemann nonreflecting far-field treatment.

## Appendix: Adjoint Equations and Gradient of the Objective Function

### Derivation of the Adjoint Equations

We associate adjoint variables

$$\boldsymbol{\lambda} = \begin{pmatrix} \lambda_1 \\ \lambda_2 \\ \lambda_3 \\ \lambda_4 \end{pmatrix}, \qquad \boldsymbol{\lambda}^b = \begin{pmatrix} \lambda_1^b \\ \lambda_2^b \\ \lambda_3^b \end{pmatrix}, \qquad \boldsymbol{\lambda}^0 = \begin{pmatrix} \lambda_1^0 \\ \lambda_2^0 \\ \lambda_3^0 \\ \lambda_4^0 \end{pmatrix}$$

with the Euler equation (3a), its BCs (3b), and initial conditions (3c), respectively. The Lagrangian corresponding to Eqs. (3a–3c) and (7) is

$$L(\boldsymbol{u}, g, \boldsymbol{\lambda}, \boldsymbol{\lambda}^b, \boldsymbol{\lambda}^0) = J(g) + \int_{t_0}^{t_f} \int_\Omega \boldsymbol{\lambda}^T \left[ \boldsymbol{q}(\boldsymbol{u})_t + \sum_{i=1}^{2} \boldsymbol{F}^i(\boldsymbol{u})_{x_i} \right] \mathrm{d}\boldsymbol{x}\, \mathrm{d}t$$
$$+ \int_{t_0}^{t_f} \int_\Gamma (\boldsymbol{\lambda}^b)^T \boldsymbol{B}(\boldsymbol{u}, \nabla \boldsymbol{u}, g)\, \mathrm{d}\boldsymbol{x}\, \mathrm{d}t$$
$$+ \int_\Gamma (\boldsymbol{\lambda}^0)^T (\boldsymbol{u} - \boldsymbol{u}_0)\, \mathrm{d}\boldsymbol{x} \tag{A1}$$

The derivative $DJ(g)$ of the objective function (7) applied to $g'$ is given by

$$DJ(g)g' = D_g L(\boldsymbol{u}, g, \boldsymbol{\lambda}, \boldsymbol{\lambda}^b, \boldsymbol{\lambda}^0) g'$$
$$= \int_{t_0}^{t_f} \int_{\Gamma_c} (\alpha_1 g_t g_t' + \alpha_2 g g' + \alpha_3 \nabla g \nabla g' + \alpha_4 \Delta g \Delta g')\, \mathrm{d}\boldsymbol{x}\, \mathrm{d}t$$
$$+ \int_{t_0}^{t_f} \int_\Gamma (\boldsymbol{\lambda}^b)^T \boldsymbol{B}_g(\boldsymbol{u}, \nabla \boldsymbol{u}, g) g'\, \mathrm{d}\boldsymbol{x}\, \mathrm{d}t \tag{A2}$$

where $\boldsymbol{\lambda}$, $\boldsymbol{\lambda}^b$, and $\boldsymbol{\lambda}^0$ are the solution of the adjoint equations $D_u L(\boldsymbol{u}, g, \boldsymbol{\lambda}, \boldsymbol{\lambda}^b, \boldsymbol{\lambda}^0)\boldsymbol{u}' = \boldsymbol{0}$ for all $\boldsymbol{u}'$. That is,

$$\int_{t_0}^{t_f} \int_\Omega (\boldsymbol{u}')^T \boldsymbol{r} + \int_{t_0}^{t_f} \int_\Omega (\boldsymbol{\lambda})^T \left[ (\boldsymbol{M}\boldsymbol{u}')_t + \sum_i (\boldsymbol{A}^i \boldsymbol{u}')_{x_i} \right]$$
$$+ \int_{t_0}^{t_f} \int_\Gamma (\boldsymbol{\lambda}^b)^T \left( \boldsymbol{B}_u \boldsymbol{u}' + \sum_i \boldsymbol{B}_{u_{x_i}} \boldsymbol{u}'_{x_i} \right)$$
$$+ \int_\Omega (\boldsymbol{u}')^T \boldsymbol{\lambda}^0 = \boldsymbol{0} \quad \forall \boldsymbol{u}' \tag{A3}$$

In Eq. (A3), $\boldsymbol{r}$ is defined by Eq. (9). Integration by parts in Eq. (A3) and variation over all functions $\boldsymbol{u}'$ leads to the equations

$$\boldsymbol{M}^T \boldsymbol{\lambda}_t + \sum_i \boldsymbol{A}^{i\,T} \boldsymbol{\lambda}^d_{x_i} = \boldsymbol{r}, \qquad (t_0, t_f) \times \Omega \tag{A4a}$$

$$\boldsymbol{\lambda} = \boldsymbol{0}, \qquad \{t_f\} \times \Omega \tag{A4b}$$

$$\boldsymbol{\lambda}^0 - (\boldsymbol{M}^T \boldsymbol{\lambda})|_{t=t_0} = \boldsymbol{0}, \qquad \{t_0\} \times \Omega \tag{A4c}$$

$$\sum_j n_j \boldsymbol{B}^T_{u_{x_j}} \boldsymbol{\lambda}^b = \boldsymbol{0}, \qquad (t_0, t_f) \times \Gamma \tag{A4d}$$

$$\sum_i n_i \boldsymbol{A}^{i\,T} \boldsymbol{\lambda}^d + \boldsymbol{B}_u^T \boldsymbol{\lambda}^b - \partial_s \sum_j s_j \boldsymbol{B}^T_{u_{x_j}} \boldsymbol{\lambda}^b = \boldsymbol{0}, \qquad (t_0, t_f) \times \Gamma \tag{A4e}$$

where, as before, $\boldsymbol{s} = (s_1, s_2)^T = (-n_2, n_1)^T$ is the unit tangential vector. For additional details on the derivation of Eqs. (A4a–A4e), see Ref 3.

Equation (A4a) gives the adjoint PDE for $\boldsymbol{\lambda}$, Eq. (A4b) specifies the final time condition for the adjoint PDE, and Eqs. (A4d) and (A4e) determine the BCs for $\boldsymbol{\lambda}$. The Eqs. (A4d) and (A4e) also determine the relation between the adjoint variables $\boldsymbol{\lambda}$ and $\boldsymbol{\lambda}^b$. Recall that $\boldsymbol{\lambda}^b$ is needed for the computation of the derivative (A2) of the objective functional. In fact, because

$$(\boldsymbol{\lambda}^b)^T \boldsymbol{B}_g(\boldsymbol{u}, \nabla \boldsymbol{u}, g) = -\lambda_1^b \tag{A5}$$

$\lambda_2^b$ and $\lambda_3^b$ are not needed. In the following, we derive the adjoint BCs for $\boldsymbol{\lambda}$ determined by Eqs. (A4d) and (A4e), as well as the relation between $\boldsymbol{\lambda}$ and $\lambda_1^b$ specified by the same equations.

Equations (11–13) state the adjoint BCs in terms of the adjoint variables $\boldsymbol{\lambda}$. For the derivation of these conditions and for their implementation, it is convenient to introduce the characteristic adjoint variables $\boldsymbol{\Psi}$, which will be defined hereafter. By $\boldsymbol{M} = \partial \boldsymbol{q}/\partial \boldsymbol{u}$, we denote the Jacobian of the conservative variables with respect to the primitive variables. We recall that $\boldsymbol{A}^i = \partial \boldsymbol{F}^i/\partial \boldsymbol{u}$. Hence, $\boldsymbol{A}^i = \partial \boldsymbol{F}^i/\partial \boldsymbol{q}\boldsymbol{M}$. It is well known (see, for example, Sec. 16.5.2 in Ref. 30) that

$$\sum_i n_i \left( \frac{\partial \boldsymbol{F}^i}{\partial \boldsymbol{q}} \right) = \boldsymbol{P} \boldsymbol{\Lambda} \boldsymbol{P}^{-1}$$

where $\boldsymbol{\Lambda}$ is a diagonal matrix with diagonal entries $\boldsymbol{v}^T\boldsymbol{n}$, $\boldsymbol{v}^T\boldsymbol{n}$, $\boldsymbol{v}^T\boldsymbol{n} + c$, $\boldsymbol{v}^T\boldsymbol{n} - c$, and

$$\boldsymbol{P} = \begin{bmatrix} 1 & 0 & \frac{\rho}{2c} & \frac{\rho}{2c} \\ v_1 & \rho n_2 & \frac{\rho}{2c}(v_1 + c n_1) & \frac{\rho}{2c}(v_1 - c n_1) \\ v_2 & -\rho n_1 & \frac{\rho}{2c}(v_2 + c n_2) & \frac{\rho}{2c}(v_2 - c n_2) \\ \frac{\boldsymbol{v}^T\boldsymbol{v}}{2} & \rho(v_1 n_2 - v_2 n_1) & \frac{\rho}{2c}(H + c\boldsymbol{v}^T\boldsymbol{n}) & \frac{\rho}{2c}(H - c\boldsymbol{v}^T\boldsymbol{n}) \end{bmatrix} \tag{A6}$$

Here, $c = \sqrt{(\gamma p/\rho)}$ denotes the speed of sound, and $H = \frac{1}{2}\boldsymbol{v}^T\boldsymbol{v} + c^2/(\gamma - 1)$ is the stagnation enthalpy. With

$$\boldsymbol{L}^{-1} = \boldsymbol{P}^{-1}\boldsymbol{M} = \begin{bmatrix} \gamma - 1/\gamma & 0 & 0 & -\rho/\gamma T \\ 0 & n_2 & -n_1 & 0 \\ c/\gamma p & n_1 & n_2 & c/\gamma T \\ c/\gamma p & -n_1 & -n_2 & c/\gamma T \end{bmatrix} \tag{A7}$$

we obtain

$$\sum_i n_i \boldsymbol{A}^{i\,T} = \boldsymbol{M}^T \sum_i n_i \left(\frac{\partial \boldsymbol{F}^i}{\partial \boldsymbol{q}}\right)^T = \boldsymbol{M}^T(\boldsymbol{P}\boldsymbol{\Lambda}\boldsymbol{P}^{-1})^T = \boldsymbol{L}^{-T}\boldsymbol{\Lambda}\boldsymbol{P}^T \tag{A8}$$

This identity, together with the definition

$$\boldsymbol{\Psi} = \boldsymbol{P}^T\boldsymbol{\lambda} \tag{A9}$$

of the characteristic adjoint variables will be used to rewrite (A4e). References 16 and 34–36 have also used adjoint characteristic variables in the formulation and implementation of adjoint BCs.

**Adjoint Wall BCs**

Because the number of imposed BCs and the imposed quantities themselves depend on the sign of the normal velocity control, we discuss suction and blowing BCs separately.

*Suction ($\boldsymbol{v}^T\boldsymbol{n} = g > 0$)*

The suction BC operator and its derivatives are given by

$$\boldsymbol{B}(\boldsymbol{u}, \nabla\boldsymbol{u}, g) = \begin{bmatrix} n_1 v_1 + n_2 v_2 - g \\ 0 \\ 0 \end{bmatrix}$$

$$\boldsymbol{B}_u = \begin{bmatrix} 0 & n_1 & n_2 & 0 \\ 0 & 0 & 0 & 0 \\ 0 & 0 & 0 & 0 \end{bmatrix}, \qquad \boldsymbol{B}_{u_{x_j}} = \boldsymbol{0}$$

By the use of Eqs. (A8) and (A9), the Eqs. (A4e) are given by

$$\begin{bmatrix} \dfrac{\gamma - 1}{\gamma} & 0 & \dfrac{c}{\gamma p} & \dfrac{c}{\gamma p} \\ 0 & n_2 & n_1 & -n_1 \\ 0 & -n_1 & n_2 & -n_2 \\ \dfrac{-\rho}{\gamma T} & 0 & \dfrac{c}{\gamma T} & \dfrac{c}{\gamma T} \end{bmatrix} \begin{bmatrix} \boldsymbol{v}^T\boldsymbol{n}\psi_1 \\ \boldsymbol{v}^T\boldsymbol{n}\psi_2 \\ (\boldsymbol{v}^T\boldsymbol{n} + c)\psi_3 \\ (\boldsymbol{v}^T\boldsymbol{n} - c)\psi_4 \end{bmatrix} + \begin{bmatrix} 0 \\ n_1\lambda_1^b \\ n_2\lambda_1^b \\ 0 \end{bmatrix} = \boldsymbol{0} \tag{A10}$$

Multiplication of the first equation in Eqs. (A10) by $p$, and subtraction from the result $T$ times the fourth equation, leads to

$$(\boldsymbol{v}^T\boldsymbol{n})\psi_1 = 0 \tag{A11}$$

The fourth equation of Eqs. (A10) and (A11) give the second adjoint BC

$$(\boldsymbol{v}^T\boldsymbol{n} + c)\psi_3 + (\boldsymbol{v}^T\boldsymbol{n} - c)\psi_4 = 0 \tag{A12}$$

If we multiply the second and third components of Eqs. (A10) by $n_2$ and $-n_1$, respectively, and add the results, we obtain

$$(\boldsymbol{v}^T\boldsymbol{n})\psi_2 = 0 \tag{A13}$$

Equations (A11–A13) are the adjoint BCs (11) stated earlier.

If we multiply the second component of Eq. (A10) by $n_1$, and the third component by $n_2$, and add the results, we obtain

$$\lambda_1^b = (\boldsymbol{v}^T\boldsymbol{n} - c)\psi_4 - (\boldsymbol{v}^T\boldsymbol{n} + c)\psi_3 \tag{A14}$$

The adjoint variable $\lambda_1^b$ is the only component of $\boldsymbol{\lambda}^b$ needed for the computation of the objective function derivative. [See Eqs. (A2) and (A5).]

*Solid Surface ($\boldsymbol{v}^T\boldsymbol{n} = g = 0$)*

On a uncontrolled solid surface, Eqs. (A11) and (A13) are identically satisfied, and only Eq. (A12) needs to be imposed.

*Blowing ($\boldsymbol{v}^T\boldsymbol{n} = g < 0$)*

In the case $\boldsymbol{v}^T\boldsymbol{n} = g < 0$, the BC operator and its derivatives are given by

$$\boldsymbol{B}(\boldsymbol{u}, \nabla\boldsymbol{u}, g) = \begin{bmatrix} n_1 v_1 + n_2 v_2 - g \\ (S - S_0)g^2 \\ (\partial_{x_2} v_1 - \partial_{x_1} v_2)g^2 \end{bmatrix}$$

$$\boldsymbol{B}_u = \begin{bmatrix} 0 & n_1 & n_2 & 0 \\ -g^2/\rho & 0 & 0 & g^2/(\gamma - 1)T \\ 0 & 0 & 0 & 0 \end{bmatrix}$$

$$\boldsymbol{B}_{u_{x_j}} = \begin{bmatrix} 0 & 0 & 0 & 0 \\ 0 & 0 & 0 & 0 \\ 0 & \delta_{2j}g^2 & -\delta_{1j}g^2 & 0 \end{bmatrix}$$

where $\delta_{ij}$ denotes the Kronecker symbol. Equation (A4e) implies

$$\lambda_3^b = 0 \tag{A15}$$

Equations (A15), (A8), and (A9) can be used to write Eq. (A4e) as

$$\begin{bmatrix} \gamma - 1/\gamma & 0 & c/\gamma p & c/\gamma p \\ 0 & n_2 & n_1 & -n_1 \\ 0 & -n_1 & n_2 & -n_2 \\ -\rho/\gamma T & 0 & c/\gamma T & c/\gamma T \end{bmatrix} \begin{bmatrix} \boldsymbol{v}^T\boldsymbol{n}\psi_1 \\ \boldsymbol{v}^T\boldsymbol{n}\psi_2 \\ (\boldsymbol{v}^T\boldsymbol{n} + c)\psi_3 \\ (\boldsymbol{v}^T\boldsymbol{n} - c)\psi_4 \end{bmatrix}$$

$$+ \begin{bmatrix} -(g^2/\rho)\lambda_2^b \\ n_1\lambda_1^b \\ n_2\lambda_1^b \\ [g^2/(\gamma - 1)T]\lambda_2^b \end{bmatrix} = \boldsymbol{0} \tag{A16}$$

Notice that the second and third components in Eq. (A16) are identical to the second and third components in Eq. (A10). Hence, we obtain Eqs. (A13) and (A14).

Another BC for $\boldsymbol{\lambda}$ is obtained from Eq. (A16). We can eliminate $\lambda_2^b$ from the first and fourth components of Eq. (A16) by multiplying these components by $\rho$ and $(\gamma - 1)T$, respectively, and add the results to obtain

$$(\boldsymbol{v}^T\boldsymbol{n} + c)\psi_3 + (\boldsymbol{v}^T\boldsymbol{n} - c)\psi_4 = 0 \tag{A17}$$

In summary, there are two BCs that need to be imposed on $\psi$, namely, Eqs. (A17) and (A13). These BCs are equivalent to Eq. (A13). As in the preceding case, the adjoint variable $\lambda_1^b$ needed for the computation of the objective function derivative [see Eqs. (A2) and (A5)] is obtained from Eq. (A14). Note that the vorticity BC of the state only leads to the condition (A15). Because it involves only derivatives of the primitive variables, this BC does not enter Eq. (A16). A consequence of this is the appearance of the additional BCs (A13).

**Gradient Computation**

Given $\lambda_1^b$, the gradient of the objective function can now be computed from Eq. (A2). Details may be found in Ref. 2.

## Acknowledgments

This work was supported in part by Texas Advanced Technology Program Grant 003604-0001-1999, National Science Foundation (NSF) Grant DMS-0075731, and the Los Alamos National Laboratory (LANL) Computer Science Institute through LANL Contract 03891-99-23 as part of the prime contract (W-7405-ENG-36) between the Department of Energy and the Regents of the University of California. Computations were performed on an SGI Origin 2000, which was purchased with the aid of NSF Grant 98-72009.

## References

[1]Sesterhenn, J., "A Characteristic-Type Formulation of the Navier–Stokes Equations for High Order Upwind Schemes," *Computers and Fluids*, Vol. 30, 2001, pp. 37–67.

[2]Collis, S. S., Ghayour, K., Heinkenschloss, M., Ulbrich, M., and Ulbrich, S., "Optimal Control of Unsteady Compressible Viscous Flows," *International Journal on Numerical Methods in Fluids*, Vol. 40, 2002, pp. 1401–1429.

[3]Collis, S. S., Ghayour, K., Heinkenschloss, M., Ulbrich, M., and Ulbrich, S., "Numerical Solution of Optimal Control Problems by the Compressible Navier–Stokes Equations," *Proceedings of the International Conference on Optimal Control of Complex Structures*, edited by G. Leugering, J. Sprekels, and F. Tröltzsch, Vol. 139, Birkhäuser Verlag, Oberwolfach, Germany, 2001, pp. 43–55.

[4]Collis, S. S., Ghayour, K., and Heinkenschloss, M., "Optimal Control of Aeroacoustic Noise Generated by Cylinder Vortex Interaction," *International Journal of Aeroacoustics*, Vol. 1, 2002, pp. 97–114.

[5]Tam, C. K. W., and Dong, Z., "Wall Boundary Conditions for High-Order Finite Difference Schemes in Computational Aeroacoustics," *Theoretical and Computational Fluid Dynamics*, Vol. 6, No. 6, 1994, pp. 303–322.

[6]Kurbatskii, K. A., and Tam, C. K. W., "Cartesian Boundary Treatment of Curved Walls for High-Order Computational Aeroacoustics Schemes," *AIAA Journal*, Vol. 35, No. 1, 1997, pp. 133–140.

[7]Joslin, R. D., Gunzburger, M. D., Nicolaides, R. A., Erlebacher, G., and Hussaini, M. Y., "Self-Contained Automated Methodology for Optimal Flow Control," *AIAA Journal*, Vol. 35, No. 5, 1997, pp. 816–824.

[8]Abergel, F., and Temam, R., "On Some Control Problems in Fluid Mechanics," *Theoretical and Computational Fluid Dynamics*, Vol. 1, 1990, pp. 303–325.

[9]Berggren, M., "Numerical Solution of a Flow-Control Problem: Vorticity Reduction by Dynamic Boundary Action," *SIAM Journal on Scientific and Statistical Computing*, Vol. 19, 1998, pp. 829–860.

[10]He, J.-W., Glowinski, R., Metcalfe, R., Nordlander, A., and Periaux, J., "Active Control and Drag Optimization for Flow Past a Circular Cylinder. I. Oscillatory Cylinder Rotation," *Journal of Computational Physics*, Vol. 163, 2000, pp. 83–117.

[11]Fursikov, A. V., Gunzburger, M. D., and Hou, L. S., "Boundary Value Problems and Optimal Boundary Control for the Navier–Stokes Systems: The Two-Dimensional Case," *SIAM Journal of Control and Optimization*, Vol. 36, 1998, pp. 852–894.

[12]Gunzburger, M. D., and Manservisi, S., "The Velocity Tracking Problem for Navier–Stokes Flows with Boundary Control," *SIAM Journal of Control and Optimization*, Vol. 39, 2000, pp. 594–634.

[13]He, B., Ghattas, O., and Antaki, J. F., "Computational Strategies for Shape Optimization of Time-Dependent Navier–Stokes Flows," Dept. of Civil and Environmental Engineering, TR CMU-CML-97-102, Carnegie Mellon Univ., Pittsburgh, PA, June 1997.

[14]Li, Z., Navon, M., Hussaini, M. Y., and Dimet, F. X. L., "Optimal Control of Cylinder Wakes via Suction and Blowing," *Computers and Fluids*, Vol. 32, No. 2, 2003, pp. 149–171.

[15]Anderson, W. K., and Venkatakrishnan, V., "Aerodynamic Design Optimization on Unstructured Grids with a Continuous Adjoint Formulation," ICASE, TR 97-9, Hampton, VA, 1997.

[16]Giles, M. B., and Pierce, N. A., "Adjoint Equations in CFD: Duality, Boundary Conditions and Solution Behavior," AIAA Paper 97-1850, 1997.

[17]Iollo, A., and Salas, M. D., "Optimum Transonic Airfoils Based on the Euler Equations," ICASE, TR 96-76, Hampton, VA, 1996.

[18]Jameson, A., and Reuther, J., "Control Theory Based Airfoil Design Using the Euler Equations," AIAA Paper 94-4272, June 1994.

[19]Nadarajah, S. K., and Jameson, A., "A Comparison of the Continuous and Discrete Adjoint Approach to Automatic Aerodynamic Optimization," AIAA Paper 2000-0667, Jan. 2000.

[20]Lele, S. K., "Compact Finite Difference Schemes with Spectral-Like Resolution," *Journal of Computational Physics*, Vol. 103, No. 1, 1992, pp. 16–42.

[21]Tam, C. K. W., and Webb, J. C., "Dispersion-Relation-Preserving Finite Difference Schemes for Computational Acoustics," *Journal of Computational Physics*, Vol. 107, 1993, pp. 262–281.

[22]Collis, S. S., "A Computational Investigation of Receptivity in High-Speed Flow Near a Swept Leading-Edge," Ph.D. Dissertation, Dept. of Mechanical Engineering, Stanford Univ., Stanford, CA, March 1997.

[23]Carpenter, M. H., Gottlieb, D., and Abarbanel, S., "Stable and Accurate Boundary Treatments for Compact, High-Order Finite Difference Schemes," *Applied Numerical Mathematics*, Vol. 12, No. 1–3, 1993, pp. 55–87.

[24]Israeli, M., and Orszag, S. A., "Approximation of Radiation Boundary Condition," *Journal of Computational Physics*, Vol. 41, 1981, pp. 115–135.

[25]Thompson, K. W., "Time-Dependent Boundary Conditions for Hyperbolic Systems," *Journal of Computational Physics*, Vol. 68, 1987, pp. 1–24.

[26]Thompson, K. W., "Time-Dependent Boundary Conditions for Hyperbolic Systems, II," *Journal of Computational Physics*, Vol. 89, 1990, pp. 439–461.

[27]Poinsot, T. J., and Lele, S. K., "Boundary Conditions for Direct Simulations of Compressible Viscous Flows," *Journal of Computational Physics*, Vol. 101, No. 1, 1992, pp. 104–129.

[28]Giles, M. B., "Nonreflecting Boundary Conditions for Euler Equation Calculations," *AIAA Journal*, Vol. 28, No. 12, 1990, pp. 2050–2058.

[29]Moretti, G., "The λ-scheme," *Computers and Fluids*, Vol. 7, 1979, pp. 191–205.

[30]Hirsch, C., *Numerical Computation of Internal and External Flows*, Vol. 2, Wiley, New York, 1990, Chap. 19.

[31]Shu, C.-W., "Esentially Non-Oscillatory and Weighted Essentially Non-Oscillatory Schemes for Hyperbolic Conservation Laws," ICASE, TR 97-65, Hampton, VA, Nov. 1997.

[32]Hager, W. W., "Runge–Kutta Methods in Optimal Control and the Transformed Adjoint System," *Numerische Mathematik*, Vol. 87, 2000, pp. 247–282.

[33]Vogel, C. R., and Wade, J. G., "Analysis of Costate Discretizations in Parameter Estimation for Linear Evolution Equations," *SIAM Journal on Control and Optimization*, Vol. 33, 1995, pp. 227–254.

[34]Sanders, B. F., and Katopodes, N. D., "Control of Canal Flow by Adjoint Sensitivity," *Journal of Irrigation and Drainage Engineering*, Vol. 125, No. 5, 1999, pp. 287–297.

[35]Sanders, B. F., and Katopodes, N. D., "Adjoint Sensitivity Analysis for Shallow-Water Wave Control," *Journal of Engineering Mechanics*, Vol. 126, No. 9, 2000, pp. 909–919.

[36]Baysal, O., and Ghayour, K., "Continuous Adjoint Sensitivities for General Cost Functionals on Unstructured Meshes in Aerodynamic Shape Optimization," *AIAA Journal*, Vol. 39, No. 1, 2001, pp. 48–55.

W. J. Devenport
*Associate Editor*